Toxicokinetics for organ-on-chip devices: Supplement

Nathaniel G. Hermann,[a] Richard A. Ficek,[a] Dmitry A. Markov,[b]
Lisa J. McCawley,[b] and M. Shane Hutson[a*]
[a] *Department of Physics and Astronomy, Vanderbilt University*
[b] *Department of Biomedical Engineering, Vanderbilt University*

Table S1: Chemical concentrations used in experiments herein and in previous studies in OOC devices.

Chemical	Cosolvent	Conc. used here (μM)	Conc. used previously (μM)	Citations
Amodiaquine	–	140	1 – 10	[1, 2]
Benzo[a]pyrene	50-70% DMSO	12 – 40	3 – 100	[3, 4, 5, 6]
Chlorpyrifos	70-90% DMSO	28	10 – 30	[7]
Fluorescein	–	0.2	100	[8]
FITC	–	2.5	1.25	[1]
Indole	0-40% DMSO	128	1 – 500	[9, 10, 11]
Paraoxon	–	120	0.1 – 200	[12, 13, 14]
Parathion	1-70% DMSO	34	0.01 – 37	[15, 16]
Rhodamine B	–	23	100	[17]
Rhodamine 6G	–	5.5	100	[17]
Acridine Orange	–	28	0.75 – 377	[18]
1,2,3-Benzotriazole	–	0.5	–	–
Benzyl Alcohol	–	1.0×10^4	–	–
Bromophenol Blue	0.8% MeOH	22	–	–
Colchicine	–	54	25	[19]
Cyclohexanol	–	3.6×10^5	–	–
Diacetone Alcohol	–	1.5×10^5	–	–
Ethofumesate	10% DMSO	352	75	[20]
Glutaraldehyde	–	138	–	–
Hexazinone	–	39	40	[20]
Imazaquin	10% DMSO	6.7	17	[20]
N-Nitrosodiphenylamine	0.7% MeOH	42	–	–
N-Nitrosodimethylamine	10% MeOH	3.2×10^3	–	–
Pentaerythritol	–	1.2×10^5	–	–

Table S2: CAS numbers and selected properties for chemicals tested. Chemical properties sourced from PubChem [21]. Reported value of logP for rhodamine 6G, bromophenol blue, FITC, acridine orange, imazaquin, and rhodamine B are computed values (XlogP).

Chemical name	CAS #	logP	H-Bond Donors	Molar Mass (amu)
Rhodamine 6G	989-38-8	6.4	2	479.0
Benzo[a]pyrene	50-32-8	6.1	0	252.3
Bromophenol Blue	115-39-9	5.8	2	670.0
Chlorpyrifos	2921-88-2	5.0	0	350.6
FITC	3326-32-7	4.8	2	389.4
Parathion	56-38-2	3.8	0	291.3
Amodiaquine	86-42-0	3.7	2	355.9
Fluorescein	2321-07-5	3.4	2	332.3
Acridine Orange	10127-02-3	3.4	0	265.4
N-Nitrosodiphenylamine	86-30-6	3.1	0	198.2
Ethofumesate	26225-79-6	2.7	0	286.4
Imazaquin	81335-37-7	2.5	2	311.3
Indole	120-72-9	2.1	1	117.2
Paraoxon	311-45-5	2.0	0	275.2
Rhodamine B	81-88-9	1.9	1	479.0
Hexazinone	51235-04-2	1.9	0	252.3
1,2,3-Benzotriazole	95-14-7	1.4	1	119.1
Cyclohexanol	108-93-0	1.2	1	100.2
Colchicine	64-86-8	1.1	1	399.4
Benzyl Alcohol	100-51-6	1.1	1	108.1
Diacetone Alcohol	123-42-2	-0.2	1	116.2
Glutaraldehyde	111-30-8	-0.3	0	100.1
N-Nitrosodimethylamine	62-75-9	-0.6	0	74.1
Pentaerythritol	115-77-5	-1.7	4	136.2

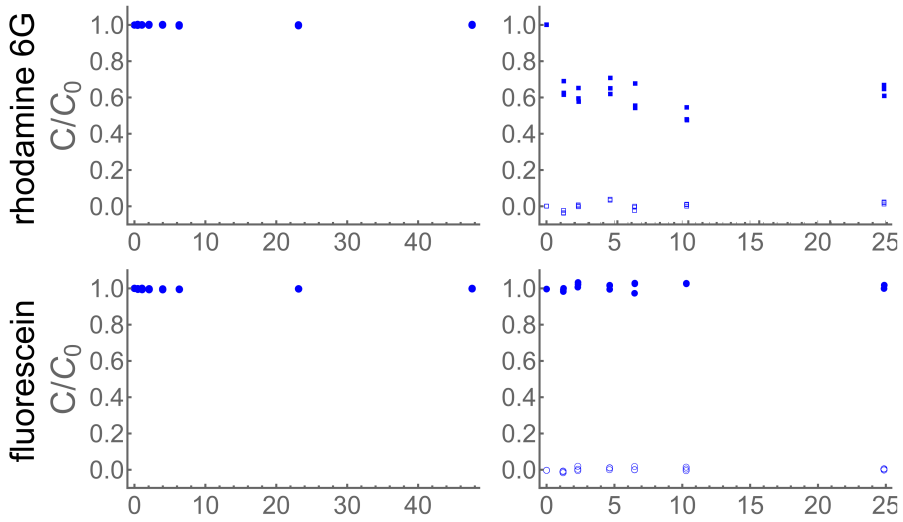

Figure S1: Disk-soak and diffusion-through-membrane results for two additional chemicals in phosphate-buffered saline: rhodamine 6G binds to the surface of PDMS, but does not diffuse into the bulk; fluorescein does not measurably interact with PDMS. Left column shows disk-soak data and associated fits (dashed). Right column shows diffusion-through-membrane results with data from both source chamber (filled symbols) and sink chamber (open symbols) with associated fits (dashed).

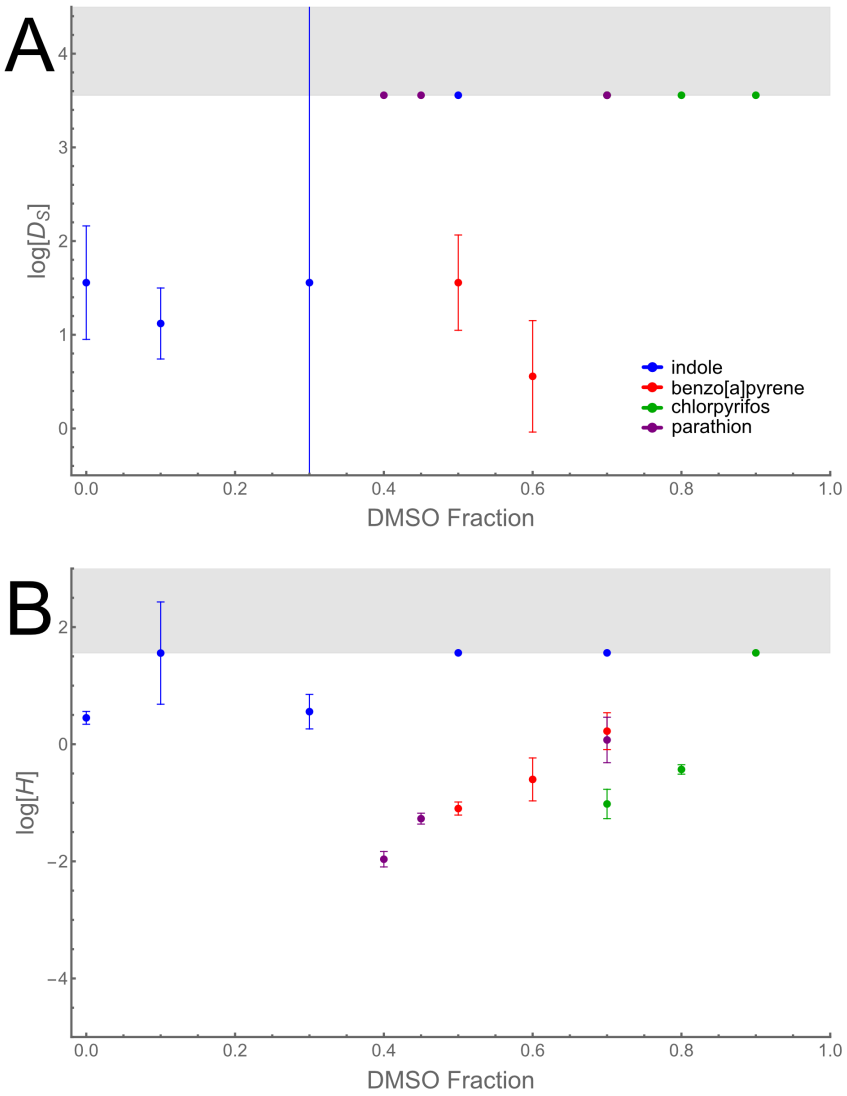

Figure S2: Best-fit values for the diffusion constants in solution, logD_S (A), and the mass-transport coefficient, log$H$ (B), for indole, benzo[a]pyrene, chlorpyrifos, and parathion at several DMSO volume fractions. Shaded regions mark regimes in which the plotted parameter is not rate limiting. Note that in (A), the rate-limiting boundary (log$D_S \approx 3.55$) has several overlapping points for different chemicals.

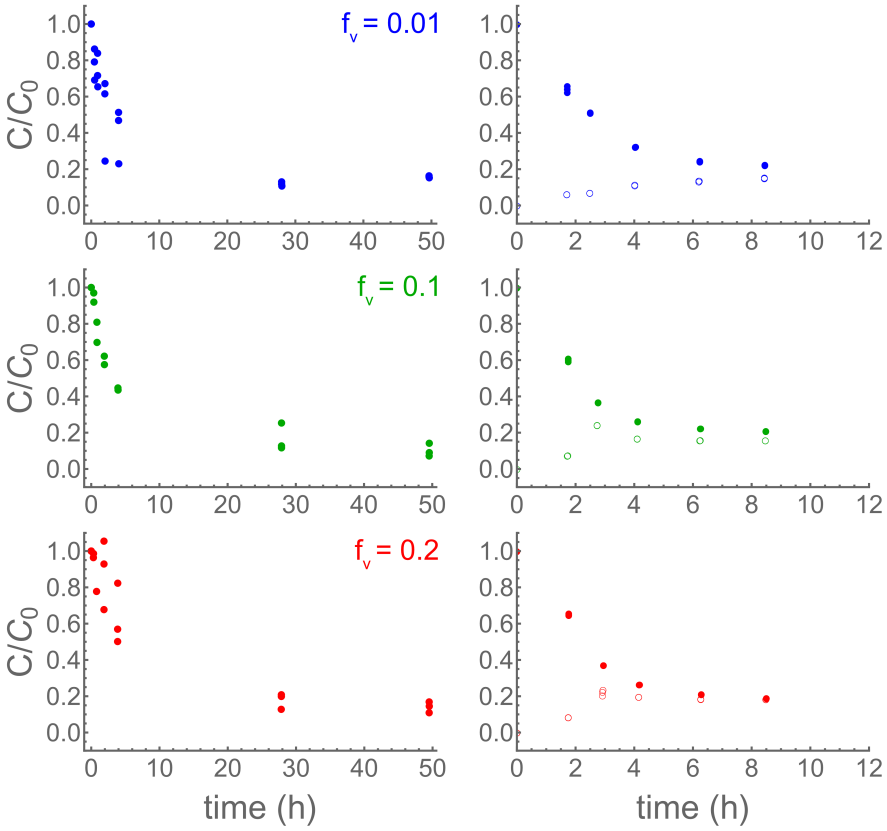

Figure S3: Experimental results from disk-soak (left) and diffusion-through-membrane experiments (right) for parathion in mixed PBS-DMSO solutions at the noted DMSO volume fractions, f_V. For disk soaks, the equilibrium concentration in all three mixed solutions is around 10% of the initial concentration; for membrane experiments, the source and sink chambers equilibrate around 20% of the initial concentration. These results indicate that saturation occurs when parathion reaches a concentration of approximately 3.2 mM in PDMS. This concentration corresponds to one parathion molecule per 520 nm^3 of PDMS, *i.e.*, approximately one molecule per $(8\ \text{nm})^3$-cube.

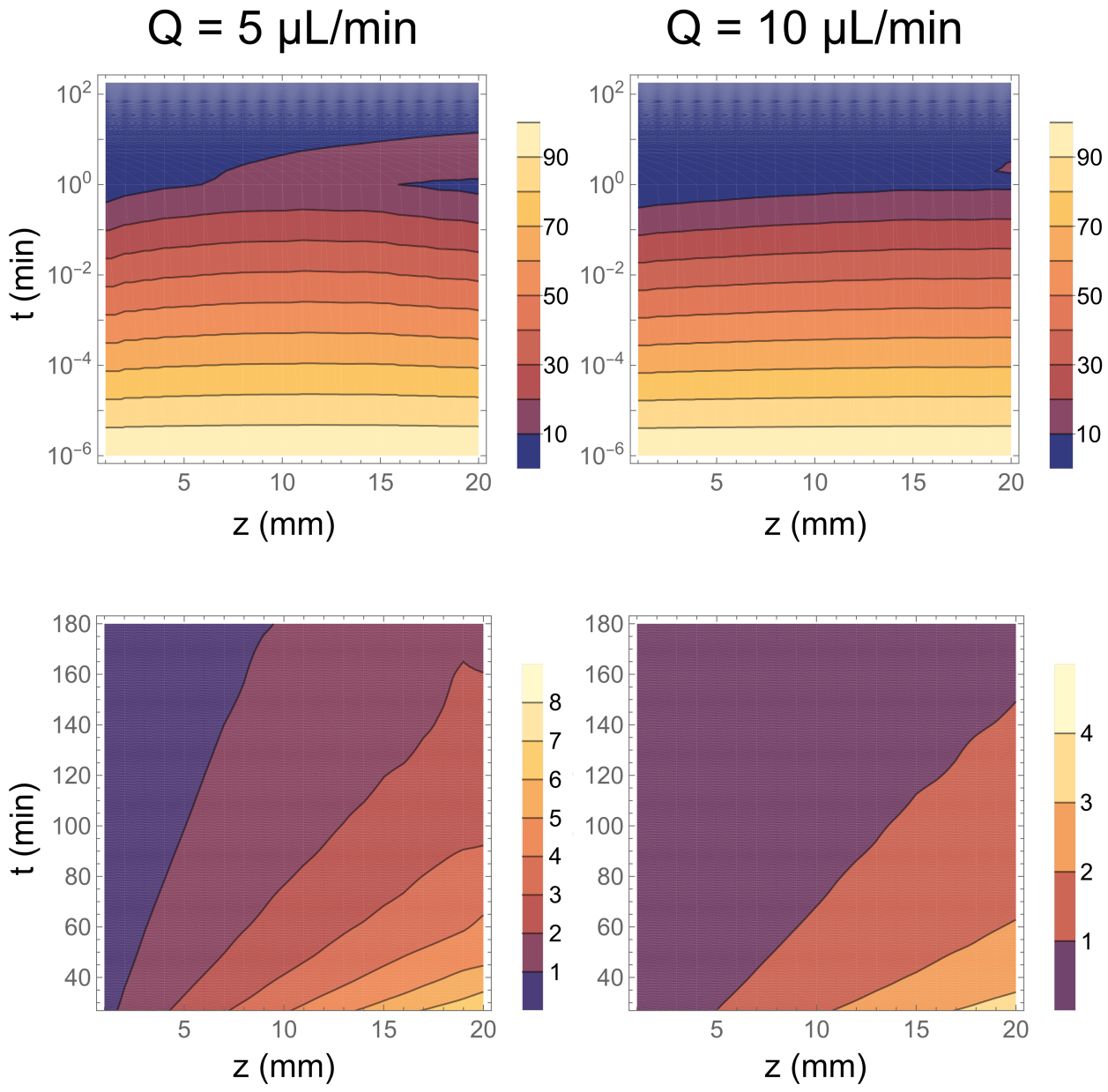

Figure S4: Contour plots of percent error of 1D heuristic model with full 3D simulation of indole flowing through PDMS microchannels at (Left) 5 μL/min and (Right) 10 μL/min. Upper plots have log-scaled time, showing increasing error at small times. Lower plots show that at long times ($\geq$ 30 min), percent error drops to below 10%, with error increasing with z.

Table S3: $\log K_{PW}$ and $\log D_P$ for seven PCBs, including two pairs of isomers. Reported values of $\log K_{PW}$ compiled and reported by Zhu et al [22]. Reported values of $\log D_P$ from Rusina et al (PCB 18, PCB 153) [23] or Belles et al. [24].

Chemical name	Num. Cl	$\log K_{PW}$	Num. studies for K_{PW}	$\log D_P$ (mm^2/h)
CB 18	3	4.93 ± 0.15	17	-0.68
CB 28	3	5.06 ± 0.20	28	-0.72
CB 52	4	5.38 ± 0.17	33	-1.06
CB 101	5	5.83 ± 0.41	25	-1.11
CB 138	6	6.20 ± 0.42	17	-1.16
CB 153	6	6.15 ± 0.60	30	-1.11
CB 180	7	6.30 ± 0.67	28	-1.17

Table S4: Calculated molecular descriptors, extrapolated $\log K_{PW}$, and $\log D_P$ for seven PBDEs, including two pairs of isomers. Extrapolated $\log K_{PW}$ ($\text{xlog}K_{PW}$) is calculated using the QSPR model developed by Zhu et al. [22] based on descriptors calculated using PaDEL: Crippen logP (cLogP); relative negative charge-most negative charge/total negative charge (RNCG); centered Broto-Moreau auto-correlation-lag 4/weighted by Sanderson electro-negativity (ATSC4e); and Geary auto-correlation-lag 6/weighted by polarizabilities (GATS6p) [25]. Values of $\log D_P$ reported by Narváez Valderrama et al. [26].

Chemical name	Num. Br	cLogP	RNCG	ATSC4e	GATS6p	$\text{xlog}K_{PW}$	$\log D_P$ (mm^2/h)
BDE 28	3	6.27	0.37	-0.80	0.94	4.43	-1.05
BDE 47	4	7.03	0.35	-0.85	0.89	5.01	-1.04
BDE 99	5	7.79	0.34	-0.64	0.88	5.59	-1.15
BDE 100	5	7.79	0.33	-0.59	0.88	5.62	-1.04
BDE 153	6	8.55	0.32	-0.48	0.90	6.17	-1.21
BDE 154	6	8.55	0.32	-0.44	0.90	6.20	-1.22
BDE 209	10	11.60	0.24	0.39	1.00	8.67	-1.24

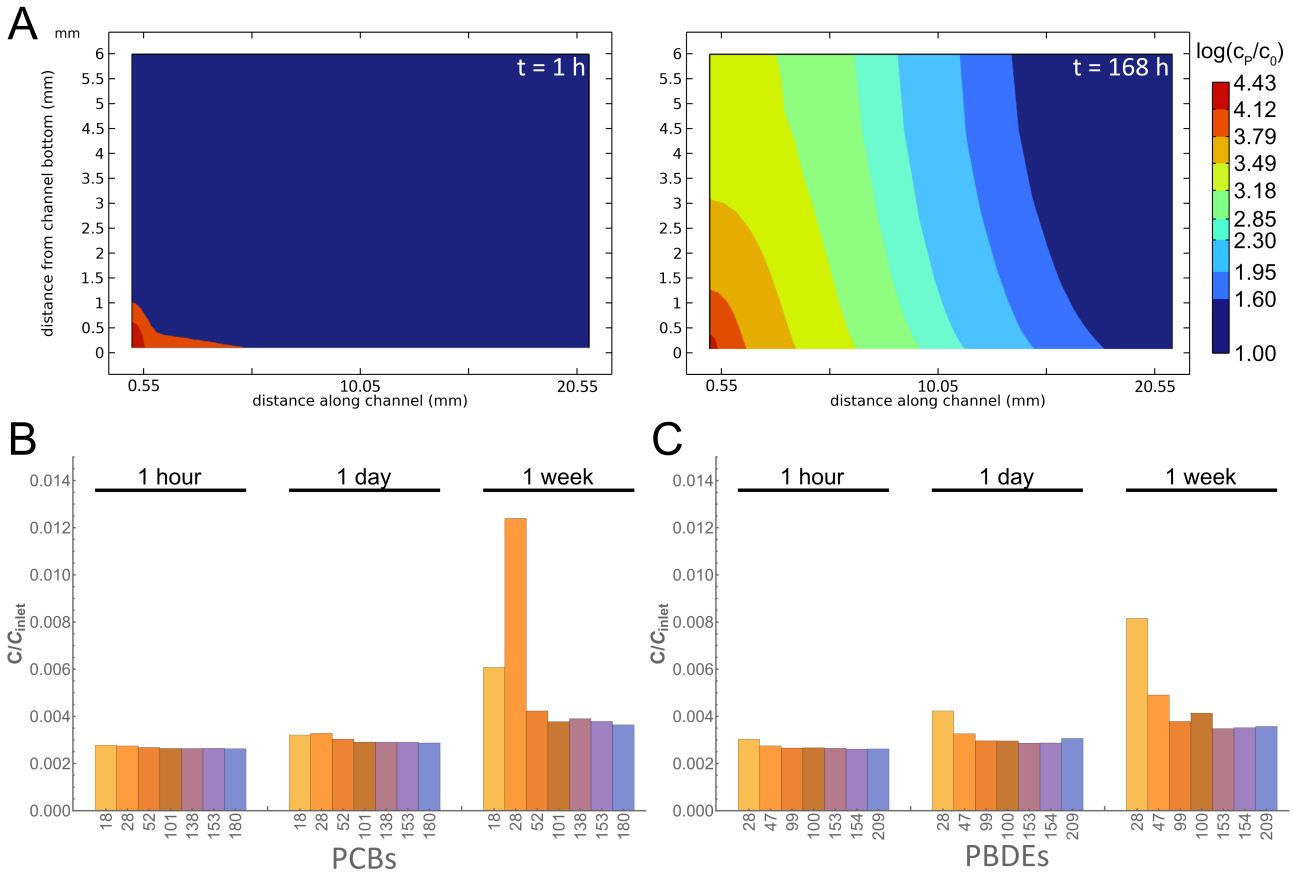

Figure S5: (A) COMSOL simulation of how PBDE 28 distributes in and around a microfluidic channel (21.1-mm long by 1.5-mm wide by 0.1-mm tall) under continuous flow (10 uL/min from left to right) after 1 hour (left) and 1 week (right). (B-C) Relative concentration remaining in solution at the end of the channel based on COMSOL simulations for seven PCBs (B) and seven PBDEs (C). Results presented after one hour, one day, and one week of continuous flow. Parameters K_{PW} and D_P for each compound were as detailed in Tables S3 and S4; solution diffusivity (D_S) was estimated via the method developed by Miyamoto and Shimono.[27] Given the large ratio of PDMS volume to channel volume and the large partition coefficients of PCBs and PBDEs, all 14 compounds are predicted to have less than 1.25% their inlet concentration remaining at the outlet, even after a week of continuous flow.

Supplemental Movies

Figure S6: (Left) Direct observation of diffusion of rhodamine B into bulk PDMS. A microchannel was pre-soaked with a rhodamine B solution for three hours to pre-load chemical into the PDMS walls. The microchannel was then flushed, and the subsequent diffusion of pre-loaded dye was imaged for 12 hours. (Right) Under similar conditions, rhodamine 6G remains on the PDMS surface and does not measurably diffuse into bulk PDMS over 12 hours.

Figure S7: Sample results from a COMSOL Multiphysics simulation of the partitioning and diffusion of indole from a solution flowing through a microfluidic channel. Flow rate was 5 µL/min over a duration of two hours, with flow direction from left to right along the bottom of the figure. Highest concentrations of indole are red; lowest are blue.

Supplemental Derivation

Suppose we have a channel filled with aqueous solution in a block of PDMS. We will say that this flow is in direction $\hat{\mathbf{z}}$. Now, we must consider the flux across the walls of the channel into bulk PDMS. This flux is in the radial direction, $\hat{\mathbf{r}}$ The flux, $\mathbf{J}$, is

$$\mathbf{J} = -\hat{\mathbf{r}} D_P \left.\frac{\partial c_P}{\partial r}\right|_{r=0}$$

Let's suppose that the mass transfer rate H is fast, such that we can approximate the surface concentration to be fixed at $c_P(r=0) = Kc_S$, where c_S is the concentration in solution and K is the PDMS-water partition coefficient. We can then say that the concentration profile in the bulk PDMS is

$$c_P(r,t) = Kc_S \text{ erfc}\left(\frac{r}{\sqrt{4D_P t}}\right)$$

Then, taking the derivative of this function, the magnitude of the surface flux must be

$$J = \frac{Kc_S\sqrt{D_P}}{\sqrt{\pi t}}$$

From this, we consider the cross-sectional perimeter, P, and area, A, of the channel, along with the flow velocity v (here assumed to be constant relative to r), and relate the change in concentration across channel slice dz to the flux

$$-Av\frac{dc_S}{dz}\Delta z = JP\Delta z = \frac{Kc_s\sqrt{D_P}}{\sqrt{\pi t}}P\Delta z$$

We will solve for the derivative and define a length constant λ,

$$\frac{dc_s}{dz} = -\frac{PKc_s\sqrt{D_P}}{Av\sqrt{\pi t}} = -\frac{1}{\lambda}c_s$$

From there, it trivially follows that the concentration at axial distance z from the channel inlet can be approximated as

$$c_S(z,t) = c_{S,0}e^{-z/\lambda}$$

where

$$\lambda = \frac{Av\sqrt{\pi t}}{PK\sqrt{D_P}} = \frac{Q\sqrt{\pi t}}{PK\sqrt{D_P}}$$

where we make one final substitution and define our familiar volumetric flow rate, $Q = Av$.

So, we can see that as K increases, D_P increases, P increases, or Q decreases, we will see a greater loss of chemical from solution. Note also that the two chemical-PDMS interaction parameters, $K\sqrt{D_P}$, are coupled, hinting that for simple devices where diffusion between channels is not a concern, a doubling in partitioning is indistinguishable from a quadrupling of diffusivity. This provides a good heuristic tool for a researcher – with only geometric knowledge of their channels and the chemical-PDMS interaction properties for their chemical-of-interest, one can estimate concentration loss anywhere within a simple device.

References

[1] Jennifer Grant, Alican Özkan, Crystal Oh, Gautam Mahajan, Rachelle Prantil-Baun, and Donald E. Ingber. Simulating drug concentrations in PDMS microfluidic organ chips. *Lab on a Chip*, 21, 2021.

[2] Longlong Si, Haiqing Bai, Melissa Rodas, Wuji Cao, Crystal Yuri Oh, Amanda Jiang, Rasmus Moller, Daisy Hoagland, Kohei Oishi, Shu Horiuchi, Skyler Uhl, Daniel Blanco-Melo, Randy A. Albrecht, Wen Chun Liu, Tristan Jordan, Benjamin E. Nilsson-Payant, Ilona Golynker, Justin Frere, James Logue, Robert Haupt, Marisa McGrath, Stuart Weston, Tian Zhang, Roberto Plebani, Mercy Soong, Atiq Nurani, Seong Min Kim, Danni Y. Zhu, Kambez H. Benam, Girija Goyal, Sarah E. Gilpin, Rachelle Prantil-Baun, Steven P. Gygi, Rani K. Powers, Kenneth E. Carlson, Matthew Frieman, Benjamin R. tenOever, and Donald E. Ingber. A human-airway-on-a-chip for the rapid identification of candidate antiviral therapeutics and prophylactics. *Nature Biomedical Engineering*, 5:815–829, 2021.

[3] Dhanuka P. Wasalathanthri, Spundana Malla, Itti Bist, Chi K. Tang, Ronaldo C. Faria, and James F. Rusling. High-throughput metabolic genotoxicity screening with a fluidic microwell chip and electrochemiluminescence. *Lab on a Chip*, 13:4554–4562, 2013.

[4] Fen Zhang, Chang Tian, Wenming Liu, Kan Wang, Yuanqing Wei, Huaisheng Wang, Jinyi Wang, and Songqin Liu. Determination of benzopyrene-induced lung inflammatory and cytotoxic injury in a chemical gradient-integrated microfluidic bronchial epithelium system. *ACS Sensors*, 3:2716–2725, 12 2018.

[5] Claire Baranger, Isabelle Pezron, Laurence Lins, Magali Deleu, Anne Le Goff, and Antoine Fayeulle. A compartmentalized microsystem helps understanding the uptake of benzo[a]pyrene by fungi during soil bioremediation processes. *Science of The Total Environment*, 784:147151, 8 2021.

[6] B. Kopp, A. Khawam, K. Di Perna, D. Lenart, M. Vinette, R. Silva, T.B. Zanoni, C. Rore, G. Guenigault, E. Richardson, T. Kostrzewski, A. Boswell, P. Van, C. Valentine III, J. Salk, and A. Hamel. Liver-on-chip model and application in predictive genotoxicity and mutagenicity of drugs. *Mutation Research - Genetic Toxicology and Environmental Mutagenesis*, 896:503762, 5 2024.

[7] Dusty R. Miller, Ethan S. McClain, James N. Dodds, Andrzej Balinski, Jody C. May, John A. McLean, and David E. Cliffel. Chlorpyrifos disrupts acetylcholine metabolism across model blood-brain barrier. *Frontiers in Bioengineering and Biotechnology*, 9:622175, 2021.

[8] Chien Fu Chen, Jikun Liu, Chien Cheng Chang, and Don L. DeVoe. High-pressure on-chip mechanical valves for thermoplastic microfluidic devices. *Lab on a Chip*, 9:3511–3516, 2009.

[9] Nicole M Vega, Kyle R Allison, Ahmad S Khalil, and James J Collins. Signaling-mediated bacterial persister formation. *Nature Chemical Biology*, 8:431–433, 5 2012.

[10] Giraso Keza Monia Kabandana, Curtis G. Jones, Sahra Khan Sharifi, and Chengpeng Chen. 3d-printed microfluidic devices for enhanced online sampling and direct optical measurements. *ACS Sensors*, 5:2044–2051, 7 2020.

[11] Xiaojing Li, Binbin Zhang, Yiyang Hu, and Yu Zhao. New insights into gut-bacteria-derived indole and its derivatives in intestinal and liver diseases. *Frontiers in Pharmacology*, 12:769501, 12 2021.

[12] Jinseok Heo and Richard M. Crooks. Microfluidic biosensor based on an array of hydrogel-entrapped enzymes. *Analytical Chemistry*, 77:6843–6851, 11 2005.

[13] Parawee Rattanakit, Gillian M. Greenway, and Saisunee Liawruangrath. Development and evaluation of microfluidic device for the determination of organophosphorus pesticide incorporating monolith based immobilized ache with spectrophotometric detection. *International Journal of Environmental Analytical Chemistry*, 93:739–754, 6 2013.

[14] Stanislav S. Terekhov, Ivan V. Smirnov, Anastasiya V. Stepanova, Tatyana V. Bobik, Yuliana A. Mokrushina, Natalia A. Ponomarenko, Alexey A. Belogurov, Maria P. Rubtsova, Olga V. Kartseva, Marina O. Gomzikova, Alexey A. Moskovtsev, Anton S. Bukatin, Michael V. Dubina, Elena S. Kostryukova, Vladislav V. Babenko, Maria T. Vakhitova, Alexander I. Manolov, Maja V. Malakhova, Maria A. Kornienko, Alexander V. Tyakht, Anna A. Vanyushkina, Elena N. Ilina, Patrick Masson, Alexander G. Gabibov, and Sidney Altman. Microfluidic droplet platform for ultrahigh-throughput single-cell screening of biodiversity. *Proceedings of the National Academy of Sciences*, 114:2550–2555, 3 2017.

[15] Donghoon Lee, Sangyeop Lee, Gi Hun Seong, Jaebum Choo, Eun Kyu Lee, Dae Gab Gweon, and Sanghoon Lee. Quantitative analysis of methyl parathion pesticides in a polydimethylsiloxane microfluidic channel using confocal surface-enhanced raman spectroscopy. *Applied Spectroscopy*, 60:373–377, 2006.

[16] Niko Amend, Marianne Koller, Christian Schmitt, Franz Worek, and Timo Wille. The suitability of a polydimethylsiloxane-based (PDMS) microfluidic two compartment system for the toxicokinetic analysis of organophosphorus compounds. *Toxicology Letters*, 388:24–29, 10 2023.

[17] Stefan Schneider, Eduardo J.S. Brás, Oliver Schneider, Katharina Schlünder, and Peter Loskill. Facile patterning of thermoplastic elastomers and robust bonding to glass and thermoplastics for microfluidic cell culture and organ-on-chip. *Micromachines*, 12:575, 2021.

[18] Cheuk-Wing Li, Jun Yang, Chi Hung Tzang, Jianlong Zhao, and Mengsu Yang. Using thermally printed transparency as photomasks to generate microfluidic structures in PDMS material. *Sensors and Actuators A: Physical*, 126:463–468, 2 2006.

[19] Gad D. Vatine, Riccardo Barrile, Michael J. Workman, Samuel Sances, Bianca K. Barriga, Matthew Rahnama, Sonalee Barthakur, Magdalena Kasendra, Carolina Lucchesi, Jordan Kerns, Norman Wen, Weston R. Spivia, Zhaohui Chen, Jennifer Van Eyk, and Clive N. Svendsen. Human iPSC-derived blood-brain barrier chips enable disease modeling and personalized medicine applications. *Cell Stem Cell*, 24:995–1005, 6 2019.

[20] Alexander W. Auner, Kazi M. Tasneem, Dmitry A. Markov, Lisa J. McCawley, and M. Shane Hutson. Chemical-PDMS binding kinetics and implications for bioavailability in microfluidic devices. *Lab on a Chip*, 19:864–874, 2019.

[21] Sunghwan Kim, Jie Chen, Tiejun Cheng, Asta Gindulyte, Jia He, Siqian He, Qingliang Li, Benjamin A. Shoemaker, Paul A. Thiessen, Bo Yu, Leonid Zaslavsky, Jian Zhang, and Evan E. Bolton. Pubchem 2023 update. *Nucleic Acids Research*, 51:D1373–D1380, 2023.

[22] Tengyi Zhu, Wenxuan Chen, Haomiao Cheng, Yajun Wang, and Rajendra Prasad Singh. Prediction of polydimethylsiloxane-water partition coefficients based on the pp-LFER and QSAR models. *Ecotoxicology and Environmental Safety*, 182:109374, 2019.

[23] Tatsiana P. Rusina, Foppe Smedes, and Jana Klanova. Diffusion coefficients of polychlorinated biphenyls and polycyclic aromatic hydrocarbons in polydimethylsiloxane and low-density polyethylene polymers. *Journal of Applied Polymer Science*, 116, 2010.

[24] Angel Belles, Christine Franke, Claire Alary, Yann Aminot, and James W. Readman. Understanding and predicting the diffusivity of organic compounds in polydimethylsiloxane material for passive sampler applications using a simple quantitative structure–property relationship model. *Environmental Toxicology and Chemistry*, 37:1291–1300, 2018.

[25] Chun Wei Yap. PaDEL-descriptor: An open source software to calculate molecular descriptors and fingerprints. *Journal of Computational Chemistry*, 32:1466–1474, 5 2011.

[26] Jhon F. Narváez Valderrama, Kine Baek, Francisco J. Molina, and Ian J. Allan. Implications of observed PBDE diffusion coefficients in low density polyethylene and silicone rubber. *Environmental Science: Processes Impacts*, 18:87–94, 2016.

[27] Shuichi Miyamoto and Kazumi Shimono. Molecular modeling to estimate the diffusion coefficients of drugs and other small molecules. *Molecules*, 25:5340, 11 2020.